Crystal growth of Cu_2ZnSnS_4 Solar Cell Absorber by Chemical Vapour Transport with I_2

D. Colombara[1*], S. Delsante[2], G. Borzone[2], J. M. Mitchels[3], K. C. Molloy[4], L. H. Thomas[4], B. G. Mendis[5], C. Y. Cummings[6], F. Marken[4] and L. M. Peter[4]

[1*]Université du Luxembourg – 41, rue du Brill - L-4422 Belvaux, Luxembourg
[2]Università degli Studi di Genova – DCCI, via Dodecaneso 31 - 16146 Genova, Italy
[3]University of Bath – Microscopy and Analysis Suite, Bath BA2 7AY, United Kingdom
[4]University of Bath – Department of Chemistry, Bath BA2 7AY, United Kingdom.
[5]Durham University – Department of Physics, Durham DH1 3LE, United Kingdom
[6]University of Southampton – Department of Chemistry, Southampton SO17 1BJ, United Kingdom

Email diego.colombara@uni.lu

Abstract

Single crystals of Cu_2ZnSnS_4 have been produced within sealed quartz ampoules via the chemical vapour transport technique using I_2 as the transporting agent. The effects of temperature gradient and I_2 load on the crystal habit and composition are considered. Crystals have been analysed with XRD, SEM, and TEM for compositional and structural uniformities at both microscopic and nanoscopic levels. The synthesized crystals have suitable (I_2-load dependent) properties and are useful for further solar absorber structural and physical characterizations. A new chemical vapour transport method based on longitudinally isothermal treatments is attempted. Based on a proposed simplistic mechanism of crystal growth, conditions for crystal enlargement with the new method are envisaged.

Keywords: B1. CZTS; B1. Kesterite; B2. Semiconducting quaternary chalcogenide; B3. Solar cell absorber; A2. Iodide vapour transport; A2. Transversal chemical vapour transport; A1. Congruent transport.

1. Introduction

In the frame of the thin film solar cells research area a new absorber compound has lately [1] gained interest due to its non-toxic low cost elemental constituents: Cu_2ZnSnS_4 (CZTS). Very promising results have recently been obtained on photovoltaic devices based on related sulfoselenide compounds deposited with an ink-based approach [2, 3], suggesting that this material might soon become competitive with $Cu(In,Ga)(S,Se)_2$ and CdTe for the production of commercial modules, due to the toxicity/availability issues affecting Cd, Te, Ga and In [4-6]. Although many studies are being performed on thin films of this material, some key questions can only be answered by studying single crystalline forms: crystal and electronic structures [7], phonon frequencies and line widths of Raman active modes and extension of the compositional homogeneity range [8]. It is therefore important to develop improved crystal growth methods.

Olekseyuk et al. [9] have found that Cu_2ZnSnS_4 melts incongruently at 1253K, crystallizing by the peritectic reaction p_4: L + β' (ZnS) → δ (Cu_2ZnSnS_4) with a composition of the liquid phase (L) far poor in ZnS and rich in Cu_2SnS_3. As a consequence it was found by Shimada et al. [10] that the crystal growth of Cu_2ZnSnS_4 from the melt results in the presence of impurity phases such as Cu_2SnS_3, ZnS and SnS, besides the quaternary chalcogenide, probably owing to segregation during the crystallization process. The solidification of a single-phase CZTS from the stoichiometric melt might be improved to some extent by the presence of a suitable seed or the action of a directional cooling, like in the Czochralski, the Bridgman-Stockbarger [11] or the gradient freezing techniques [12]. Single crystals of the Cu_2FeSnS_4-Cu_2ZnSnS_4 pseudobinary series were synthesized by Bernardini et al. [13] for structural investigations using the salt-flux technique reported by Moh et al. [14]. A similar approach was also employed by Altosaar et al. [15] and Timmo et al. [16] who successfully crystallized $Cu_2Zn_{1-x}Cd_xSn(Se_{1-y}S_y)_4$ and $Cu_2ZnSnSe_{4-x}S_x$ powders from molten KI with the intent of fabricating monograin layer devices [17]. The difficulty of producing the sulfur end member in a pure form was highlighted, since the X-ray Energy Dispersive Spectroscopy (EDS) analysis of the polished crystals pointed to the

presence of the secondary phases alongside the dominating CZTS phase. At the time of writing this manuscript Nagaoka et al. [18] have demonstrated the possibility to obtain primary CZTS crystals by a Sn-poor liquid phase in the Sn-Cu_2ZnSnS_4 pseudobinary system at 900 °C. CZTS single crystals of reasonable dimensions were first produced by Nitsche et al. [19] with the Chemical Vapour Transport (CVT) technique employing I_2 as the transporting agent (with low loading); the crystals were reported to be black needles with dimensions of up to 20 mm x 0.2 mm x 0.2 mm. Compositional analysis was not reported, but structure refinement from X-Ray Diffraction (XRD) revealed the compound to crystallize in a tetragonal lattice with $a = b = 5.427$ Å and $c = 10.848$ Å [20]. Nitsche's CVT results have only now been outclassed in terms of crystal thickness by Levcenko et al. [21] who succeeded in growing black blade shape crystals up to 5 mm x 1.5 mm x 1 mm.

Among the techniques for the growth of single crystals, the CVT has generally the advantage of employing lower operational temperatures and static configurations of the growing ampoule, the main drawbacks being the incorporation of the gaseous solvent species to some extent and the sensitivity of the technique to subtle variations of the growth conditions. The importance of fluid dynamics in determining the right growth conditions in such systems is well described by the literature [22-32]. The CVT crystal grower will often encounter dimensionless numbers such as the Grashof, Schmidt, Prandtl and Rayleigh numbers that serve for the description of the system, especially with regard to diffusion and convection. The interested reader is referred to Klosse's work [23] for a detailed treatment of such aspects. For example, for simple systems it is known that crystallographic perfection is favoured under diffusion-limited transport rate, when nucleation density is minimized [24]. However, due to the pentanary nature of our system, the formation of compositionally well-defined sinks is subject to the risk of incongruent transport [33].

In the present work, single crystals of Cu_2ZnSnS_4 were grown under two different I_2 loads. The effects of the temperature gradient on their habit, structure and composition were considered and growth mechanisms are discussed. A new chemical vapour transport method based on longitudinally isothermal treatments is also introduced which may be of interest for crystal enlargement in the absence of artificially-induced temperature gradients. Microscopic and nanoscopic uniformities of the crystals have been assessed with Scanning Electron Microscopy (SEM)/ X-ray EDS, and Transmission Electron Microscopy / Selected Area Electron Diffraction / Electron Energy Loss Spectroscopy (TEM)/SAED/EELS. It is shown that crystals of high quality are obtained (in particular at lower I_2 loading) suitable for more advanced structural and physical characterizations.

2. Experimental

2.1 Apparatus for the crystal growth.

The equipment employed for the crystal growth experiments consists of a custom made horizontal tubular furnace (Elite Thermal Systems Ltd.) with four independent controllers, each of which allows configuring with individual setpoints and ramp rates. In the standard experimental configuration the system is intended to provide two zones of different temperatures, with as short a transition zone as possible between them. In order to ensure the most uniform temperature within each zone, the settings of the independent controllers were chosen after careful calibration with a test thermocouple drawn along the tube inside a "dummy" quartz ampoule, thus emulating the desired experimental conditions as close as possible. The experiments were performed within sealed quartz ampoules of 23 mm internal diameter about 160 mm long. During the experiments the ampoule seats on the walls of the furnace, an alumina work tube of 30 mm internal diameter, as it is shown in Fig. 1.

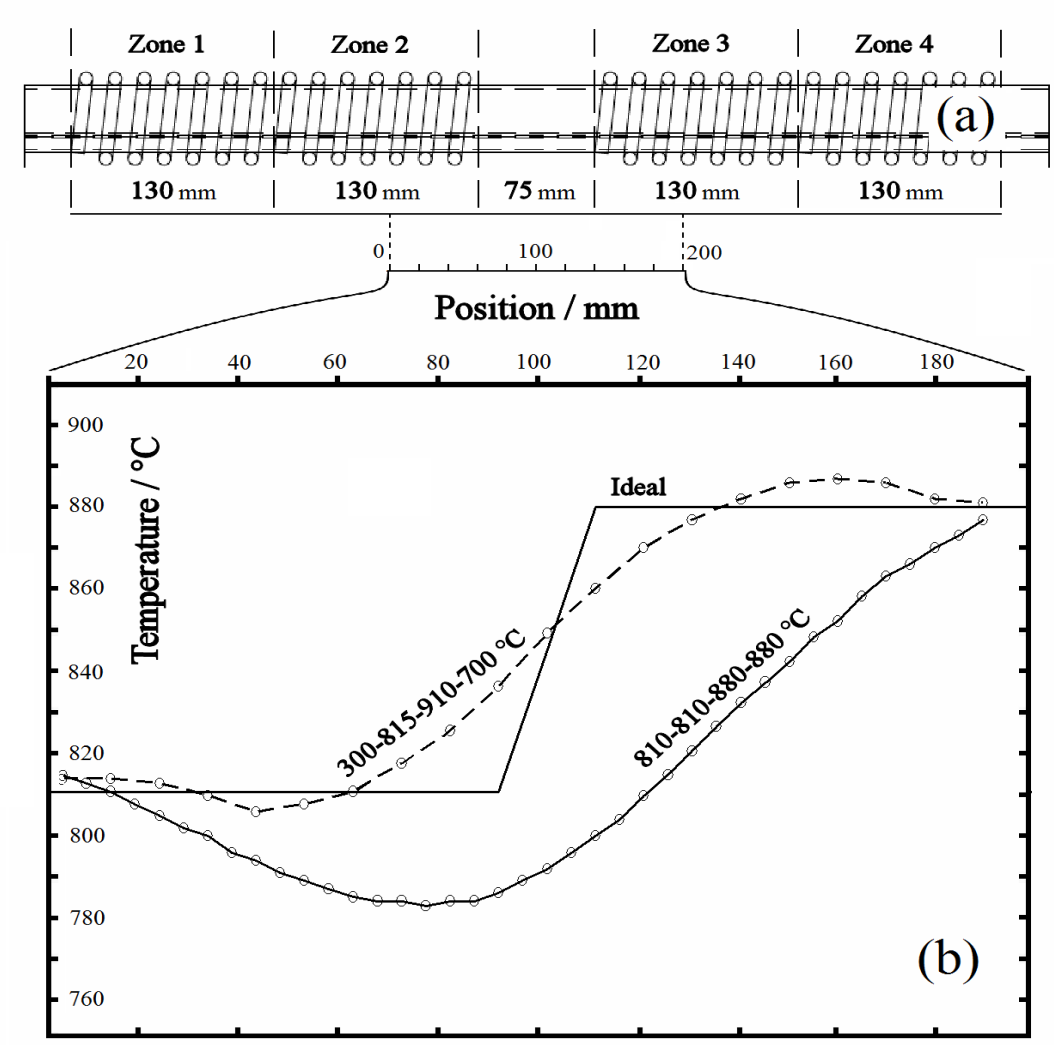

Fig. 1 Schematic representation of our four-zone oven (a) with the ideal (810-880 °C), and experimental temperature profiles obtained in the 20 cm long central part with different furnace settings (b).

Fig. 1 shows also the temperature profile along the ampoule, as measured with the thermocouple, at an unrefined and a refined stage, compared to an "ideal" condition. The unheated central part of the furnace requires the controllers of zones 2 and 3 to operate at higher temperatures than expected from the ideal profile. As a consequence, zones 1 and 4 have to operate at lower temperatures acting as radiation wells, in order to avoid overheating of the ends of the ampoule. The optimized profiles show temperature uniformity on the order of ± 5 °C over 50-60 mm long plateaus.

2.2 Pre-treatment and crystal growth

Stoichiometric amounts of 5N purity Cu, Zn, Sn and an excess (1.5 ×) of sulfur were finely ground together in an agate mortar and pressed to form green (i.e. raw) pellets. The excess sulfur was employed with the intent of preventing any deviation from stoichiometry in the early stages of the treatment (evacuation and elemental reaction), similarly to Prabukanthan et al. [34]. The pellets were then sealed within evacuated quartz ampoules and put in the tubular furnace which was gradually heated up to 700°C and left for about 48 hours, similarly to Bernardini et al. [13] and Schorr et al. [35]. The thus-obtained sinter-annealed products were used as source materials for some crystal growth experiments with the addition of the I_2 load in quartz ampoules connected to a Schlenk line where several vacuum and inert gas (N_2, Ar or He) purge steps were performed up to the final background pressure of $5 \cdot 10^{-4}$ bar, before sealing off.

First a strong temperature gradient was applied, as reported by Hönes et al. [36], so that all the precursor material reacts with the transporting agent and it is transported towards the cold end of the ampoule to form a cluster homogenized at the atomic scale (Fig. 2a). Secondly, a reversed temperature gradient of chosen magnitude was applied (Fig. 2b).

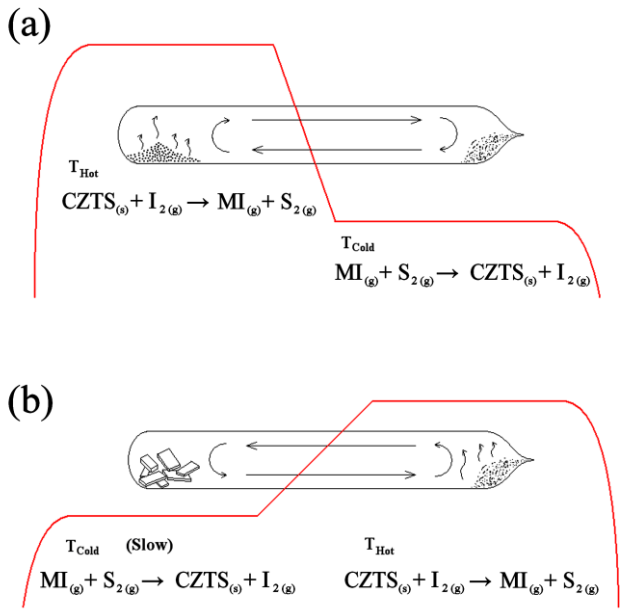

Fig. 2 Scheme of the CVT process sequence of (a) pre-synthesis with high temperature gradient and (b) actual crystal growth with the refined, reversed temperature gradient.

The effects of temperature gradient and two different I_2 loads on the crystal habit and composition were explored. Table 1 gives an overview of the main growth parameters investigated in this work together with the essential results for each run. To assist the reader, a comprehensive list of experimental conditions and results for the sole tests discussed in detail in sect. 3 is provided separately in Table 2.

Test	Duration /days	T_1 /°C	T_2 /°C	ΔT/deg	I_2 load /gcm^{-3}	Filling gas	Habit and average size	Notes
1	7	880	810	70±5	$5{\cdot}10^{-3}$	N_2	Edge-defined grains (2 mm); amorphous or microcristalline	Complete transport
2	2	880	810	70±5	$5{\cdot}10^{-3}$	N_2	Edge-defined grains (1-2 mm); amorphous or microcristalline	Complete transport
3	2	850	810	40±5	$5{\cdot}10^{-3}$	N_2	Edge-defined grains (2-3 mm); dendritic and elongated crystals (up to 10 mm); amorphous or microcristalline	Complete transport
4	1	880	750	130±5	$5{\cdot}10^{-3}$	N_2	Dendritic crystals (1-2 mm)	Incomplete transport
5	3	840	840	0±5	$5{\cdot}10^{-3}$	N_2	Lustrous wafer-thin (1-2mm)	Res. of test 3 used
6	4	820	750	70±5	$5{\cdot}10^{-3}$	N_2	Amorphous or microcrystalline	Complete transport
7	3	820	760	60±5	$5{\cdot}10^{-3}$	N_2	Amorphous or microcrystalline	Complete transport
8	2	820	770	50±5	$5{\cdot}10^{-3}$	N_2	Amorphous or microcrystalline	Complete transport
9	3	880	750	130±5	$9{\cdot}10^{-4}$	N_2	Thin needles (4 mm)	Incomplete transport
10	3	850	810	40±5	$9{\cdot}10^{-4}$	N_2	Prisms (2 mm) formed at 840°C	Incomplete transport
11	3	870	820	30±5	$9{\cdot}10^{-4}$	N_2	Microcrystalline mass	Incomplete transport
12	3	880	750	130±5	$9{\cdot}10^{-4}$	Ar	Amorphous or microcrystalline	Incomplete transport
13	7	880	750	130±5	$5{\cdot}10^{-3}$	He	Cluster of polycristals	Complete transport
14	1	790	740	50±5	$5{\cdot}10^{-3}$	He	Cluster of polycristals	Incomplete transport

Table 1 Summary of the synthesis trials with main parameters considered: duration, source and growth temperature, gradient, background filling gas. Essential experimental results for each run such as resulting crystal habit and average size, as well as mass transport completeness are also included.

2.3 Compositional and structural characterization

The materials resulting from growth tests No. 3 and 9 were fully analyzed compositionally and morphologically either with an INCA XACT X-ray EDS system connected to a Jeol 6480LV SEM or with an INCA 300 Electron Probe Micro-Analysis (EPMA) connected to a Zeiss EVO 40 SEM (Carl Zeiss SMT Ltd., Cambridge). EDS was conducted using a 1nA probe at 25 keV, all acquisitions were performed a compositional standard used for further optimisation. Samples larger than 2 mm were embedded in Taab Hard LV resin and polished up to a 0.1 μm alumina finish (Streuers) with a Metaserv rotary polishing machine for more accurate estimation of the bulk composition via SEM-X-ray EDS, as described elsewhere [37]. The same samples were also loaded on a Reichert-Jung ultramicrotome for production of thin sections (< 90 nm). The blocks and ultramicrotome were cooled using liquid nitrogen to minimise local heating of the samples. The slices were analysed with a JEOL JEM1200EXII TEM for Selected Area Electron Diffraction (SAED) and further X-ray EDS analyses using an Oxford Instruments INCA Energy 350 system. Images were acquired using a Gatan Dual View Camera. Featured diffraction measurements were confirmed using a Jeol 2100F at 200 keV. Other crystals were either Ar ion-milled in a Gatan precision ion-polishing system (PIPS) using a 3-5 kV beam and 6-8 degree gun angle, or crushed between mica foils and the fine resulting powder analysed at the TEM (JEOL 2100F FEG) for information on the compositional and structural homogeneity. Due to beam instability, the diffraction and elemental analyses were performed using a Gatan double tilt cryoholder cooled to 77 K and the current density was kept below 15 $pA \cdot cm^{-1}$. Analysis of the diffraction patterns was conducted using Gatan Digital Micrograph and Image J. Determination of the lattice parameters of the single crystals was performed with a Bruker Nonius Kappa CCD diffractometer.

3. Results

The volatile components taking part to the chemical vapour transport are most conceivably the iodides of Cu, Zn and Sn, and the elemental sulfur vapour. In such circumstances, the crystallization of Cu_2ZnSnS_4 may occur through reaction (1) from the gaseous species.

(1) $$2CuI_{(g)} + ZnI_{2\,(g)} + SnI_{4\,(g)} + 2S_{2\,(g)} \rightarrow Cu_2ZnSnS_{4\,(s)} + 4I_{2\,(g)}$$

Such overall reaction is likely to be an approximation of what may well be a series of more complicated reaction steps. Nonetheless, under the conditions investigated, the transport was found to occur from higher to lower temperatures, suggesting a negative enthalpy associated to (1). Among the empirical growth conditions investigated and summarised in Table 1 and Fig. 3, the experiments that resulted in the synthesis of single crystalline material of reasonable size (major axis > 2 mm) are No. 3 and 9. Characterizations of these crystal products is summarised in Figs. 4 and 5, respectively. The resulting data is summarised in more detail in Table 2 together with data from experiments No. 5 and 12 and the examination of the transport residues from experiment No. 9.

Test No.	**3 (growth) T_2**	**5 (isothermal)**	**9 (growth) T_2**	**9 (source) T_1**	**12 (growth) T_2**
Background gas	N_2	N_2	N_2	N_2	Ar
Duration / days	2	3	3	3	3
T_1 /°C	850	840	-	880	880
T_2 /°C	810	840	750	-	750
ΔT /deg	40±5	0±5	130±5	130±5	130±5
I_2 load / gcm^{-3}	$5 \cdot 10^{-3}$	$5 \cdot 10^{-3}$	$9 \cdot 10^{-4}$	$9 \cdot 10^{-4}$	$9 \cdot 10^{-4}$
I_2 load / precursor load (molar ratio)	2.48	2.48	0.44	0.44	0.44
Grashof number	$4.8 \cdot 10^4$	0	$5.0 \cdot 10^3$	n/a	$5.0 \cdot 10^3$
Schmidt number	1.82	1.82	1.79	n/a	1.79
Rayleigh number	$8.7 \cdot 10^4$	0	$9.0 \cdot 10^3$	n/a	$9.0 \cdot 10^3$
Longitudinal diffusive share of transport [23]	0.19	∞	0.59	n/a	0.59
Source material employed	Green pellet	Result of experiment 3	Pre-treated pellet	Pre-treated pellet	Pre-treated pellet
Habit	Elongated crystals free from the ampoule's walls	Wafer-thin lustrous crystals attached to the	Thin needles free from the ampoule's walls	Hemispherical lump attached to the ampoule's	Amorphous or microcrystalline mass

	and edge-defined crystals	ampoule's walls		walls	
Mean size / mm	2-3	1-2	4	3	< 0.5
Composition (SEM-EDS)	$Cu_{2.0}Zn_{1.0}Sn_{1.0}S_{4.0}$ $Cu_{2.2}Zn_{1.0}Sn_{2.4}S_{10.4}$ CuI, ZnS	n/a	$Cu_{1.9}Zn_{0.9}Sn_{1.0}S_{4.1}$ CuI	$Cu_{2.0}Zn_{<0.1}Sn_{1.0}S_{3.0}$ CuS CuI	n/a
Lattice parameters (XRD)	a = b = 5.421(1) Å c = 10.819(3) Å volume = 318 $Å^3$ α = β = γ = 90 ° c/(2a) = 0.998	n/a	a = b = 5.4290(2) Å c = 10.8340(4) Å volume = 319 $Å^3$ α = β = γ = 90 ° c/(2a) = 0.998	n/a	n/a
Lattice parameters (SAED)	a = b= 5.55 Å c = 10.52 Å volume = 324 $Å^3$ α = β = γ = 90 ° c/(2a) = 0.948 (at 77 K)	n/a	a = b = 5.67 Å c = 11.48 Å volume = 369 $Å^3$ α = β = γ = 90 ° c/(2a) = 1.012 (at 298 K)	n/a	n/a
Relevant figures	3a, 4a-i	3b	3c, 5a-c,h-i	3d, 5d-g	3e
Relevant literature of CZTS lattice parameters from different synthesis routes (XRD)	CVT single crystal: a=b= 5.427, c=10.848, volume= 319 $Å^3$				Schäfer et al. [20] (1974)
	CVT single crystal: a=b= 5.435, c=10.843, volume= 320 $Å^3$				Guen et al. [38] (1979)
	Salt flux single crystal: a=b= 5.434(1), c=10.856(1), volume= 320 $Å^3$				Bonazzi et al. [39] (2003)
	Powder sol. st. reaction: a=b= 5.428(2), c=10.864(4), volume= 320 $Å^3$				Schorr et al. [35] (2007)

Table 2. Summary of transport conditions and results for the most significant growth experiments (No. 3, 5, 9 and 12) and compositional/structural properties of the relevant materials obtained (n/a= not applicable/analysed). The CZTS lattice parameters as from relevant XRD literature are also reported for comparison. For computation of the fluid numbers, the reader is referred to Klosse's work [23].

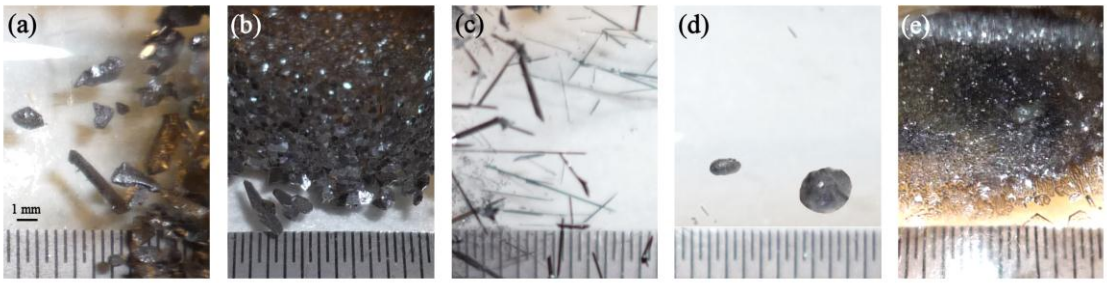

Fig. 3 Zoomed pictures of the materials resulting from the growth experiments listed in Table 2: experiments No. 3 (a), 5 (b), 9 at T_2 (c), 9 at T_1 (d) and 12 (e).

3.1 Growth with iodine load of $5 \cdot 10^{-3}$ gcm^{-3}

Fig. 4 shows collections of images relative to this growth experiment (No. 3). Fig. 4a shows the visual appearance of the ampoule at the end of the growth test. Fig. 4b shows the morphology of a typical edge-defined grain crystal, a reasonably even 3D growth was obtained. Part of the crystal surface is depicted in Fig. 4c, where the compositional variation is highlighted by the EDS mapping of the emission lines of the relevant elements under a 20 keV electron beam ($K_{\alpha1(Cu)}$, $K_{\alpha1(Zn)}$, $L_{\alpha1(Sn)}$, $K_{\alpha1(S)}$, $L_{\alpha1(I)}$). The resulting picture shows the presence of three phases: a substrate phase consistent with the composition Cu_2ZnSnS_4 (brown), covered by crystals of ZnS (orange) and CuI (blue).

In order to get more insights into the growth mechanism, some of the crystals were embedded in hard resin and polished on random orientations as to examine the core morphology and composition. The micro-scale compositional uniformity was assessed on the carbon coated specimens via Backscatter Electron Composition imaging and EDS point analyses at the SEM. The cross sectional morphology of the crystals shows that the bulk structure is rather defective with abundant voids of size up to 20 µm. A CASINO V2.42 [40] simulation of the 20 keV electron beam trajectories in bulk Cu_2ZnSnS_4 was run in order to estimate the interaction volume that defines the spatial resolution of the point EDS analyses (Fig. 4d). The microprobe analyses performed this way on numerous points randomly distributed reveal a standard deviation lower than 1 at. % for each element present. A pure cobalt standard was used for

the optimisation of the collection conditions. Evidence of the high compositional uniformity is given by the back-scattered electron (BSE) micrograph shown in Fig. 4g which was taken deliberately at very high contrast in order to enhance the compositional variation. The comparison with the secondary electron image in Fig. 5f shows contrast attributable to polishing artefacts rather than elemental inhomogeneity.

The nano-scale compositional uniformity was estimated via TEM-EDS on 90 nm thin slices of crystals cleaved from the embedded samples. Morphological analysis at the TEM shows the presence of domains with different contrast on the order of 20 nm; however, no appreciable compositional and structural differences were revealed either by EDS or SAED. TEM-EDS analyses performed at room temperature under beam currents higher than 25 $pAcm^{-1}$ revealed compositions that were consistently poorer of Sn and S in the ratio 1:2 compared to the SEM-EDS analyses. This is consistent with the evolution of $SnS_{(g)}$ and $S_{2(g)}$ from $Cu_2ZnSnS_{4(s)}$ in high vacuum [41] due to local heating by overexposure to the high energy electron beam (120 keV). Due to this unavoidable reaction, only the Cu:Zn compositional ratio can be considered as a reliable figure. Such ratio was found to be roughly 2:1. If the specimens were kept cool in a double-tilt filter at 77 K, no change in composition was observed even after prolonged beam exposure and the SAED interrogation revealed a consistent tetragonal structure throughout the samples.

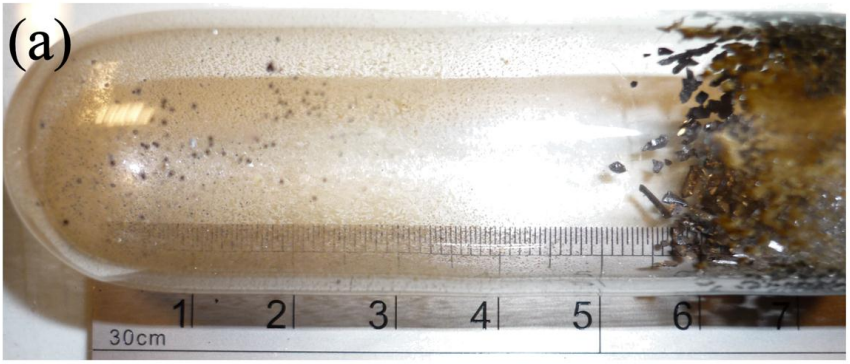
(a)
1
2
3
4
5
6
7
30cm

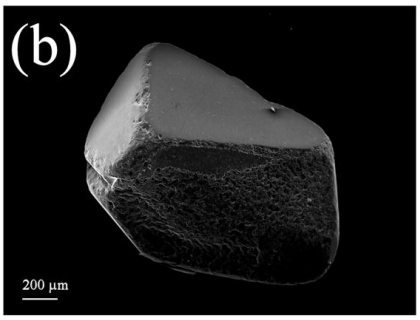
(b)
200 µm

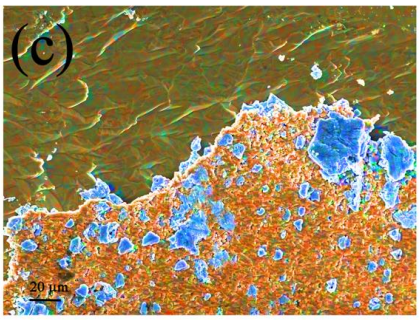
(c)
20 µm

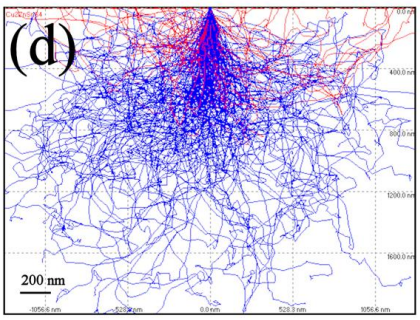
(d)
200 nm

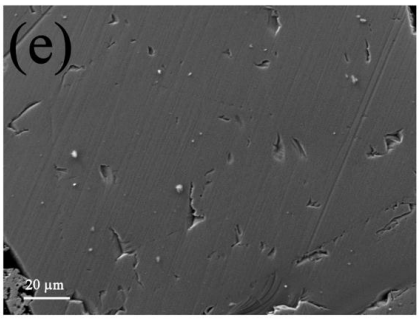
(e)
20 µm

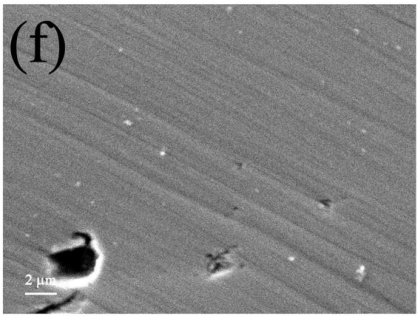
(f)
2 µm

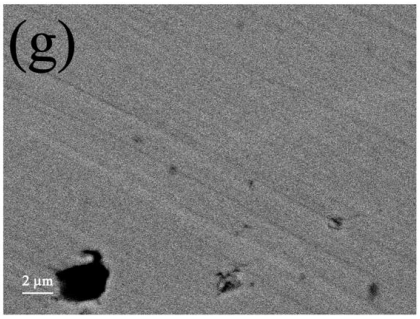
(g)
2 µm

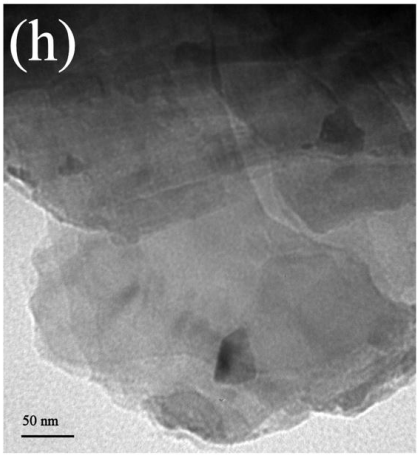
(h)
50 nm

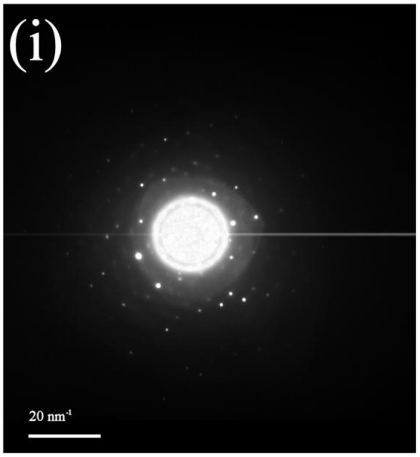
(i)
20 nm-1

Fig. 4 Collection of images relative to the growing test No. 3 (cfr. Table 2, Fig. 3a). View of the quartz ampoule at the end of experiment (a). SEM micrograph of a typical edge-defined crystal (b) and EDS compositional map of its surface (c) (blue: CuI; orange: ZnS; brown: Cu_2ZnSnS_4). CASINO V2.42 [40] simulation of interaction volume for 20 keV electrons with bulk Cu_2ZnSnS_4 (d). SEM micrograph of a polished crystal as seen from secondary electron (e-f) and BSE (g) detectors. TEM bright field micrograph of 90 nm thin slices of a crystal (h) with its SAED pattern at 77 K (i).

3.2 Growth with iodine load of $9 \cdot 10^{-4}$ gcm^{-3}

Fig. 5 shows collections of images relative to this growth experiment (No. 9). Fig. 5a shows the visual appearance of the ampoule at the end of the growth test. Fig. 5b-c shows the morphology of the needle-shaped crystals of the growing test No. 9 with typical neat edges and elongated shape (1D predominance). As for the growing test No. 3, traces of CuI crystals could be detected on the samples surface, although in smaller amount.

Fig. 5i is the SAED pattern of the ion-milled crystal on the [-110] zone axis. The diffraction is consistent with previously reported tetragonal forms of CZTS. The Kikuchi lines were highly visible during tilting from one zone axis to another, revealing that the sample was thick enough to be unaffected by the electron beam in such conditions. Figs. 5d-f are SEM-BSE micrographs of the hemispherical residue left at the source side of the quartz ampoule at the end of the transport experiment (lasted 3 days). It is possible to distinguish clearly four areas with different signal intensity. The black areas are voids and Fig. 6d shows that such porosity is concentrated in the inner part of the lump, with pores that extend radially towards the surface, delimiting grains with elongated shape.

The EDS spectra of the three remaining areas are reported in Fig. 5g. The highly scattering brittle phase (white) has composition consistent with the formula CuI (with ~ 10 at. % O contaminations), the dominant grey phase has formula Cu_2SnS_3 (with residues of I < 1 at. %) and the low scattering phase (dark grey) is consistent with CuS (with Al and I contaminations < 2 at. %). The outer surface of the lump is surrounded by a 40 µm thick crust of CuI, which is also present in the bulk of the lump filling the spaces left by the dominant Cu_2SnS_3 phase. The CuS phase shows a high degree of porosity and is segregated over a band area in the middle of the dominant Cu_2SnS_3 phase between the voids in the centre of the lump and the outer surface. A gradient of Zn concentration was found in the Cu_2SnS_3 phase from the inner to the outer part of the hemispheric lump, with a remarkable Zn concentration up to 6 at. % in the area between the CuI outer crust and the CuS-rich band, as shown in Fig. 6e.

Despite the low heating rate employed, the pre-treatment of the source material caused the Zn to be partially lost, owing probably to the large volume of the ampoule employed (same dimensions as for the crystal growth) [42]. Interestingly, under the growth conditions of experiment No. 9, in spite of the off-stoichiometry of the source material, the crystals grown at the cold end of the ampoule have composition consistent with the formula Cu_2ZnSnS_4, and no traces of the ternary Cu_2SnS_3 were found.

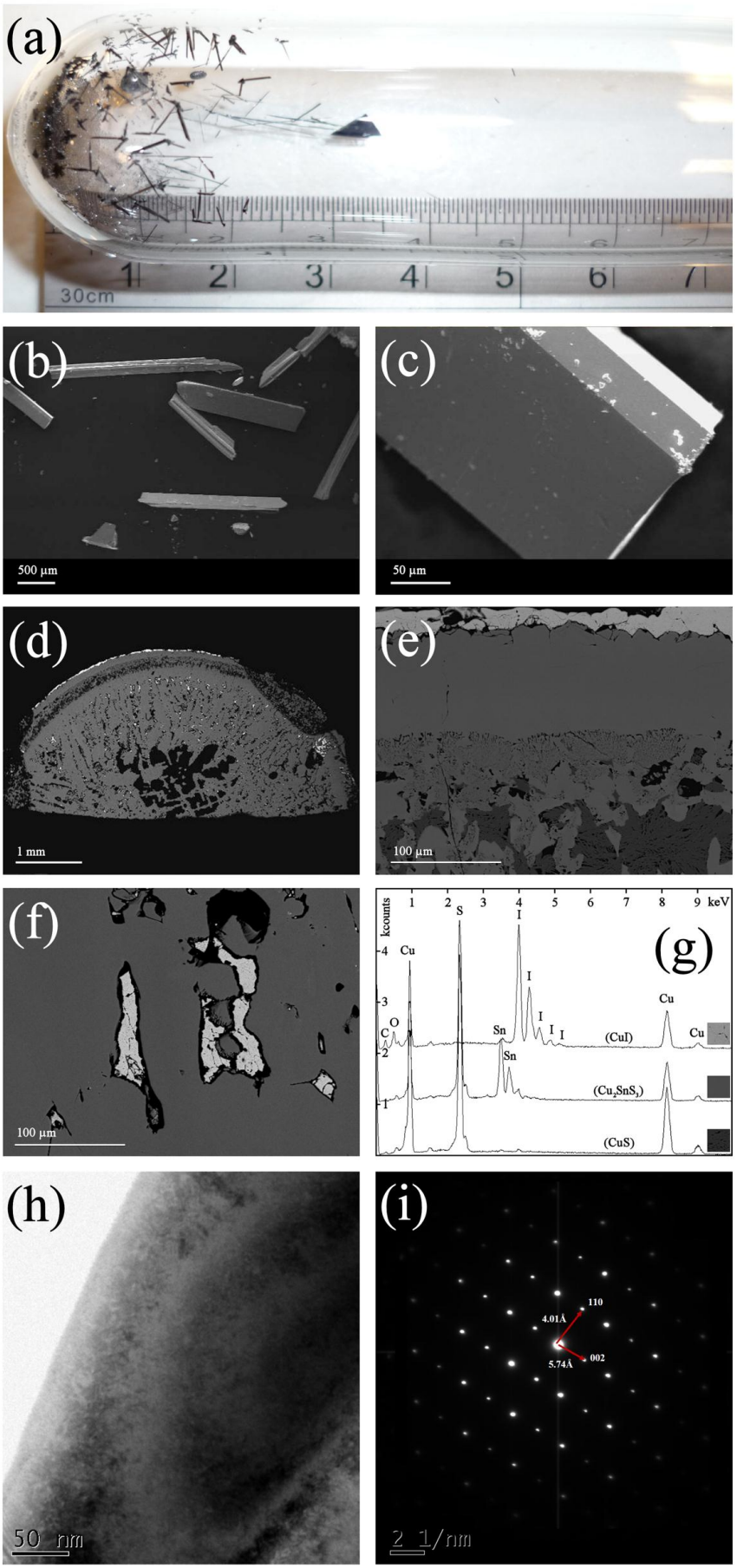
(a)
30cm
(b)
500 µm
(c)
50 µm
(d)
1 mm
(e)
100 µm
(f)
100 µm
(g)
kcounts
keV
Cu
O
C
S
Sn
I
(CuI)
(Cu2SnS3)
(CuS)
(h)
50 nm
(i)
110
4.01Å
002
5.74Å
2 1/nm

Fig. 5 Collection of images relative to the growing test No. 9 (cfr. Table 2, Fig. 3c). View of the quartz ampoule at the end of experiment (a). SEM micrographs of typical needle shaped crystals (b-c). Cross sectional BSE micrographs of the hemispherical residue left at the hot end (d-f) with pronounced compositional contrast between the three phases present for which EDS spectrum with a 20 keV electron beam is reported (g).TEM bright field image of the edge of an ion-milled crystal (h) and its SAED pattern on the [-110] zone axis nominally at room temperature (i).

4. Discussion

The structural characterizations via X-ray and electron diffractions (Table 2) reveal that the CZTS samples crystallize in tetragonal unit cells, consistently with the reported literature on this compound. The difference between the lattice parameters estimated with the two techniques is no surprise and has to do with the larger error uncertainty generally associated with the electron diffraction technique. The tetragonality factors c/(2a), obtained from the X-ray diffraction analyses point towards a unit cell that is slightly compressed along the [001] crystallographic direction, if compared to the literature values where this factor exceeds unity [35], but they are substantially in agreement with more recently reported figures [43, 44]. The CZTS samples obtained under lower I_2 pressure show slightly larger unit cells which is consistent with literature data.

In all experiments the crystallization of material (reaction (1)) occurred at the position of the ampoule corresponding to the minimum of the longitudinal temperature profile for each run, as assessed with the quartz dummy reactor. This suggests a negative enthalpy change associated to reaction (1). However, it is noticeable that such crystallization occurred preferentially on the walls of the ampoule for test No. 3 (Figs. 3a, 4a) and free from them for test No. 9 (Figs. 3c, 5a). Quenching of these two growing tests at regular time intervals followed by observation of the ampoules revealed two different means of transport. For test No. 3 a series of decomposition/crystallization steps took place throughout the length of the ampoule, while test No. 9 showed a direct transport from the hottest to the coldest end of the ampoule. From a rough estimation of the ampoule pressure for the two cases, this behaviour seems consistent with the predictions of Zuo et al. [45] on the transition between a diffusion-dominated to a convection-dominated regime of mass transport. Indeed, the computed Grashof, Schmidt and Rayleigh fluid numbers (Table 2) [23] show that the longitudinal convective share of transport for test No. 3 is about three times higher than for test No. 9. However, according to the analytical model of Klosse et al. [23], the mass transport regime should be considered convection-dominated for both these two cases. Furthermore, the Rayleigh numbers exceed $4 \cdot 10^3$, a value above which a strong deterioration of the crystal quality has been reported by Böttcher et al. [25]. This seeming contradiction must be explained on the basis of the applicability range of Klosse's model [23]. As already pointed out elsewhere [24], with iodine concentrations below certain values, the transport rate is likely to be governed by the rate of heterogeneous reaction of source vaporisation, rather than by diffusion, regardless of the temperature gradient applied. We believe that this is most probably the case for test No. 9.

With the intent to ascertain whether it is possible to enlarge the bigger crystals at the expense of the smaller ones on the same principle of the Ostwald ripening [46], an isothermal treatment at 840 °C was conducted on the resulting mass of experiment No. 3 (test No. 5, cfr. Table 2). If the "ideal equilibrium" were to be reached, this should correspond to one, nearly perfect crystal. The treatment was prolonged up to three days and lead to the formation of highly lustrous wafer-thin edge-defined crystals with average size 1-2 mm, which adhered strongly to the ampoule's walls (2D predominance). It is apparent that the dynamic decomposition/crystallization equilibrium in place transported the mass towards the walls of the ampoule, rather than contributing to the growth of bulk crystals (free from the walls). Indeed, relatively large crystals with pronounced development in the three dimensions (experiment No. 3, cfr. Fig. 3a) were slowly eroded and converted into crystals where the third dimension is strongly reduced (Fig. 3b). This situation is opposite to that described by Szczerbakow et al. [47] in the self-selective vapour growth of bulk crystals. The inversion of the sign of the growth rate observed in experiment No. 5 (namely, the crystal consumption) deserves some attention. Thermodynamically, the lower the temperature the higher is the driving force for crystallization. Therefore, a well formed crystal pointing towards the inner part of the ampoule, where the temperature is lower, should act as a good self-seed. Further growth should take place on its surface, until all the smaller, more defective crystals on the ampoule's surface are thoroughly consumed. In order to explain this different behaviour we shall analyse a plausible mechanism of crystal growth.

Fig. 6 shows a schematic representation of the consequences of CVT under longitudinally isothermal conditions (e.g experiment No. 5, cfr. Table 2). The two scenarios with different directions of transport are depicted in proximity of the ampoule's walls respectively towards (a) and from (b) a well-developed crystal. In general we can expect that the transversal profiles of temperature and thermal conductivity across the media in the closed ampoule and the pressure of free transporting agent have an effect on the thermodynamics ($\Delta G°$) and kinetics ($\Delta G^{\neq}$) of the crystallization reaction. As a first approximation we can assume that reaction (1) proceeds via absorption of unary iodide molecules onto the surface of the system, followed by collision with sulfur molecules (or vice versa), leading to the release of iodine and the formation of a binary sulfide nucleus. Due to the entropy reduction, spontaneous chemisorptions are associated to a negative enthalpy change. This means that colder surfaces are thermodynamically more convenient for this step to take place. Furthermore, according to the transition-state theory [48], the transition-state complex that forms when two molecules react has an enthalpy greater than the sum of the enthalpy of the reagents or the sum of the enthalpy of the products. Its high energy content makes the stability of the transition-state complex strongly affected by the local temperature. Overall, both these hypothetic steps for the formation of binary sulfide nuclei are exothermic and are therefore favoured by lower surface temperature. However, due to the exothermic nature of the process, local temperature is bound to rise if heat is not effectively dissipated to the surrounding. Reduction of the rate of crystal growth as growth proceeds is a known phenomenon. For example, in conventional vapour growth methods like the Piper-Polich [49] and the Markov-Davydov [50] this self-limiting behaviour is attributed to the fact that the growth front is located at the hottest part of the crystal and is therefore bottle-necked by the heat transfer through the volume of the material being grown (which is determined by its thermal conduction properties) [47].

When $RT > \Delta G^{\neq}$ and under longitudinally isothermal conditions, a dynamic equilibrium tend to be established, where the rate of crystallization equals the rate of decomposition. If the heat flux away from the crystal is lower than the flux directed towards its surface arising from crystallization, the local temperature will rise until it exceeds the temperature of the ampoule's walls, at which point the direction of transport is inverted. Under these circumstances, if the thermal conductivity of the material being grown is lower than that of the ampoule's walls the crystal is inherently unstable and bound to fully deplete at the time when the dynamic equilibrium is reached. A net material transport occurs from the crystals free from the walls to the ampoule's walls.

In steady state conditions, the decomposition/crystallization rate is ultimately dependent on the concentrations of free I_2 and S_2 in the system. Higher iodine loads correspond to higher decomposition/crystallization rates of CZTS. Since heat is released in the vicinity of the process when reaction (1) is taking place, more heat needs to be exchanged per time unit if higher iodine loads are employed. Depending on the relative resistance to heat transfer of the material being grown and the vessel, as a consequence of the local temperature variation induced by the reaction, the activation free energy for process (a) will be more or less affected than (b) by the concentration of free I_2 in the ampoule. In general, there will be a limiting iodine pressure corresponding to a steady state decomposition/crystallization rate for which the local temperature of the crystal free from the walls equals the temperature of the ampoule's walls. We call this limiting pressure # (Fig. 6). For pressures higher than # crystallization shall occur on the surface of the ampoule's walls (Fig. 6b), while pressures lower than # shall give rise to crystal enlargement (Fig. 6a).

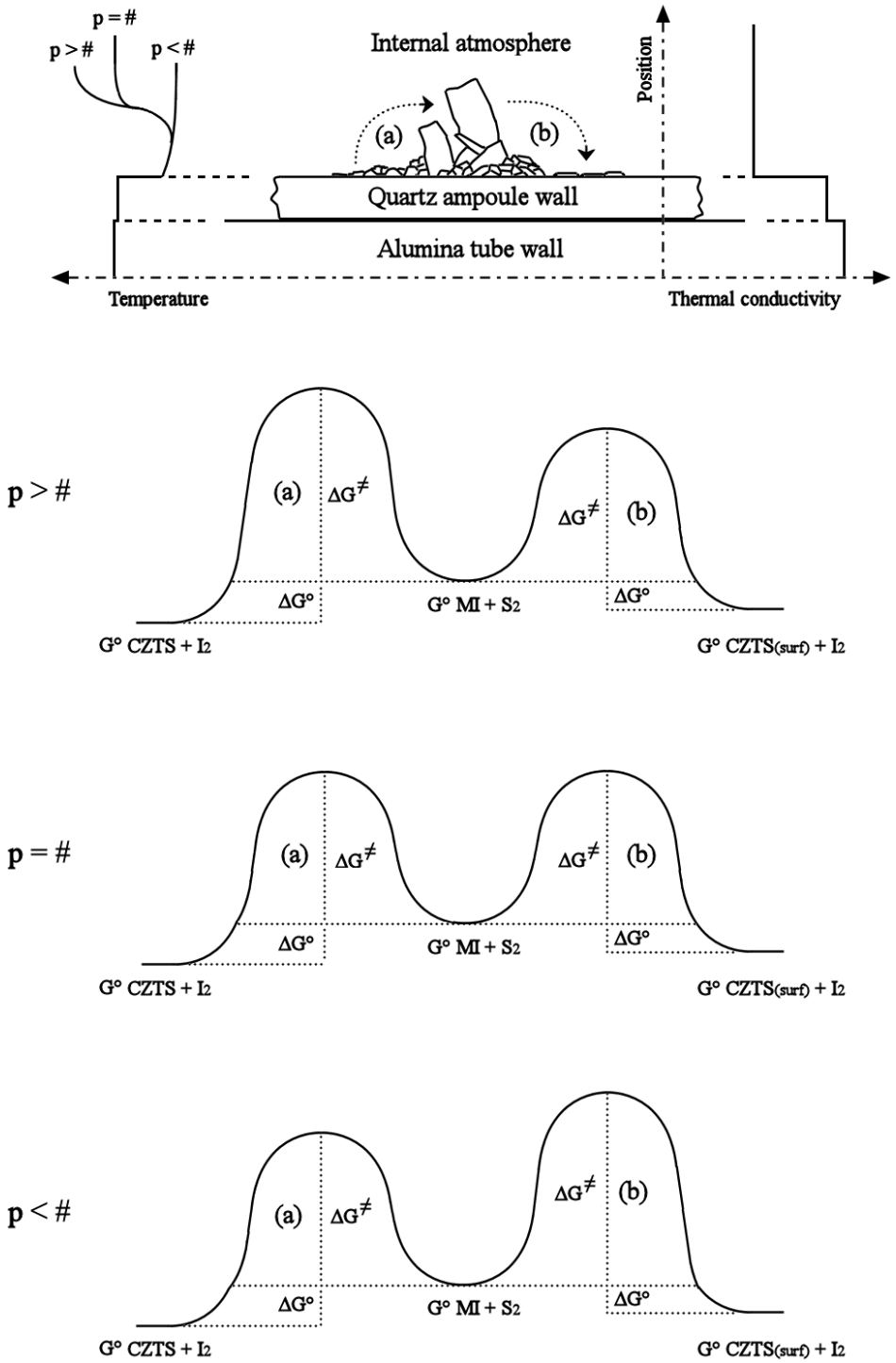

Fig. 6 Chemical vapour transport scenarios (a-b) during longitudinally isothermal treatment (e.g. test No. 5 cfr. Table 2, Fig. 3b). The figure depicts the geometry of the experiment in proximity of the ampoule's walls with transversal profiles of temperature and thermal conductivity (in this example the thermal conductivity of the material being grown is chosen lower than that of the quartz ampoule). The experimental observation for the two different transport phenomena is summarised by the simplistic free energy paths reported. If the pressure of free transporting agent exceeds a limiting value #, crystallization via path (b) prevails on (a) and vice versa.

In our experimental setup the transversal profile of thermal conductivity is such that a more efficient heat extraction can be attained by the ampoule's walls rather than by large crystals surrounded by the complex mixture of reacting gases (Fig. 6). For experiment No. 5, carried out at 840 °C with an iodine load of $5 \cdot 10^{-3}$ gcm^{-3}, this is translated into a faster kinetics for crystallization on the ampoule's walls (Fig. 6b) rather than on the surface of already formed crystals (Fig. 6a), despite the expected lower bulk temperature of such crystals.
This proposed mechanism gives also a plausible explanation as to why bulk CZTS crystals free from the walls were obtained at all during experiment No. 3. Such crystals were formed before the steady state equilibrium was reached, i.e. when part of the I_2 was sequestered by the material to be transported from the higher temperature end of the ampoule, giving rise to a lower effective decomposition/crystallization rate. Similarly, it is explained why with lower initial I_2 loads (test No. 9, cfr. Table 2, Figs. 3c, 5a) the crystallization occurred preferentially free from the ampoule's walls rather than at their surface. Experiment No. 12 (cfr. Table 2, Fig. 3e) was run under the same conditions of experiment No. 3 but using Ar instead of N_2 as the background gas. This choice lead to the formation of an amorphous or microcrystalline mass, consistently with a lower thermal conductivity of the atmosphere inside the ampoule [51].

At the end of the experiment performed with lower I_2 load (No. 9), the mass transport was found incomplete. EDS microstructure analyses were performed on the residues of the source material (sect. 3.2) in order to gain information on the mechanism of CVT (Fig. 5d-g). The interpretation that can be drawn is as follows. Under the growth conditions (T_1 = 880 °C) the Zn poor CZTS precursor is mainly liquid (m.p. Cu_2SnS_3 ~ 837 °C [52]). This allows the Zn atoms (limiting reagent) to diffuse easily through the droplet towards the surface where they are captured by the $I_{2\,(g)}$ to form $ZnI_{2\,(g)}$. The other metals also react with iodine and the formation of nearly stoichiometric CZTS at the cold end withdraws the mixture of gaseous iodides until there is enough Zn to be extracted from the source. The CuI formed by reaction of the CZTS precursor with I_2 is liquid at the test temperature (m.p. = 605 °C [52]). During cooling, the matrix of Cu_2SnS_3 crystallizes in elongated grains, the molten CuI remains trapped at the grain boundaries and the shrinkage due to its solidification causes this phase to be surrounded by voids. The Zn concentration gradient left over in the source material is opposite to what it would be expected if Zn were to be selectively leached. Indeed, due to the heterogeneous reaction occurring at the interface between gaseous I_2 and condensed source material, such phenomenon would likely lead to a Zn poor surface and a Zn rich core. There appears to be no obvious explanations for such observation. No traces of ZnI_2 (b.p = 726 °C), SnI_4 (b.p = 353 °C) and SnI_2 (b.p = 717 °C) were found in the solid residue of the source material, as their boiling points are lower than the solidification temperature of Cu_2SnS_3. The fact that these iodides are not detected at the cold end too, suggests that their stabilities is lower (higher reactivity) compared to that of CuI. Despite the Zn deficiency of the source material, no Cu_2SnS_3 was found at the cold end of the ampoule. This suggests that, to a reasonable extent, the system shows the tendency to self-adjust the crystal growth as to produce the most stable phase (in this case Cu_2ZnSnS_4) so long as sufficient amounts of each component (e.g. Zn) are available at the source end. Indeed, comparison of the EDS analyses of the main (CZTS) sinks for experiments No. 3 and 9 reveal that the composition is nearly unaffected by the I_2 pressure within the ampoules (cfr. Table 2), although increased amounts of secondary phases were detected when the larger I_2 load was employed.

5. Conclusion

High quality single crystals of Cu_2ZnSnS_4 solar absorber materials have been synthesized from the elements via the Chemical Vapour Transport in the presence of I_2. In agreement with simpler systems, it was found that an increase of the initial iodine load has a strong effect on the transport mechanism, with a transition from a diffusion (reaction-limited) to a convection-dominated regime [25]. In turn, this was found to affect significantly the shape and quality of the crystals. Highly crystalline CZTS with needle-shape (1D predominance) was obtained with $9 \cdot 10^{-4}$ gcm^{-3} of I_2, while more defective but larger crystals (3D predominance) were obtained with a nearly five-fold load. In the first case a gradient of 130 °C was employed to speed up the process and achieve well-formed crystals, while in the second case a gradient of 40 °C was necessary as larger gradients lead to the formation of polycrystalline material. There appears to be no meaningful effect of the iodine pressure employed on the composition of the CZTS samples. However, XRD analysis shows that samples obtained under

lower I_2 pressure have slightly larger unit cells. Neutron diffraction and Raman spectroscopy analyses would be required in order to ascertain if the crystals obtained under different pressure conditions have significant structural differences. These two techniques are crucial, due to the great complexity of the phase identification for the Cu-Zn-Sn-S system solely by XRD [41, 43, 53, 54].

The samples showed high compositional uniformity at the SEM/EDS/BSE level. The nanoscale compositional uniformity may be better investigated with more sophisticated transmission electron techniques. These would also add important information on the defect nature of the samples.

New CVT treatments in the absence of longitudinal temperature gradients were carried out with the aim of increasing the size of already formed crystals. Under the investigated conditions, the nucleation and growth of CZTS on the ampoule's walls (2D predominance) was kinetically more convenient than the enlargement of pre-existing CZTS crystals pointing towards the interior of the ampoule (3D predominance). A schematic crystallization reaction mechanism is proposed to account for the experimental observations. Under longitudinally isothermal CVT, based on our argument we can conclude as follows.

- With high transporting agent loads the position on the system's surface corresponding to the most effective path for heat extraction is likely to show the fastest crystallization kinetics, because self-inhibition occurs elsewhere due to local temperature variation (induced by the enthalpy of reaction).
- Under lower transporting agent pressures (i.e. with lower decomposition/crystallization rates) local temperature variation is negligible and the direction of crystallization dictated by the sign of the enthalpy of compound transport follows the naturally occurring transversal profile of temperature within the system.

More studies are required in order to confirm our hypothesis and establish the conditions for which CZTS crystal enlargement/improvement via chemical vapour transport in isothermal treatments can be made feasible. The influence of ampoules made of more insulating materials or, vice versa, the increase of the thermal conductivity of the atmosphere within the ampoule, might help making this process kinetically viable. Alternatively, formation of large CZTS crystals may be possible by a two stage CVT process where crystals free from the walls are first produced under high iodine loads with longitudinal temperature gradient quenched before the attainment of the steady state equilibrium, followed by a second longitudinally isothermal treatment performed with a lower iodine load. It is hoped that this new CVT approach will encounter the interest of the crystal growers' community.

An estimation of the temperature at which the crystal growth reaction of CZTS becomes thermodynamically spontaneous would be beneficial for the design of the growth experiments. In future, thermochemical and computational investigations could give important additional information.

Acknowledgements

Phil Jones is gratefully acknowledged for providing the quartz/glass joints and for his glassblowing experience required for sealing off the ampoules. Funding was provided by EPSRC (Supergen: Photovoltaic Materials for the 21st Century EP/F029624/1).

References

[1] H. Katagiri, N. Sasaguchi, S. Hando, S. Hoshino, J. Ohashi, T. Yokota, Preparation and evaluation of Cu2ZnSnS4 thin films by sulfurization of E---B evaporated precursors, Solar Energy Materials and Solar Cells, 49 (1997) 407-414.
[2] T.K. Todorov, K.B. Reuter, D.B. Mitzi, High-Efficiency Solar Cell with Earth-Abundant Liquid-Processed Absorber, Advanced Materials, 22 (2010) E156-E159.
[3] D.A.R. Barkhouse, O. Gunawan, T. Gokmen, T.K. Todorov, D.B. Mitzi, Device characteristics of a 10.1% hydrazine-processed $Cu2ZnSn(Se,S)_4$ solar cell, Progress in Photovoltaics: Research and Applications, 20 (2012) 6-11.
[4] B.A. Andersson, Materials availability for large-scale thin-film photovoltaics, Progress in Photovoltaics: Research and Applications, 8 (2000) 61-76.

[5] L.M. Peter, P.J. Dale, J.J. Scragg, G. Zoppi, I. Forbes, New routes to sustainable photovoltaics: evaluation of Cu_2ZnSnS_4 as an alternative absorber material, Physica Status Solidi (b), 245 (2008) 1772-1778.
[6] C. Wadia, A.P. Alivisatos, D.M. Kammen, Materials Availability Expands the Opportunity for Large-Scale Photovoltaics Deployment, Environmental Science & Technology, 43 (2009) 2072-2077.
[7] K. Tanaka, Y. Miyamoto, H. Uchiki, K. Nakazawa, H. Araki, Donor-acceptor pair recombination luminescence from Cu2ZnSnS4 bulk single crystals, physica status solidi (a), 203 (2006) 2891-2896.
[8] K. Muska, M. Kauk, M. Altosaar, M. Pilvet, M. Grossberg, O. Volobujeva, Synthesis of Cu_2ZnSnS_4 monograin powders with different compositions, Energy Procedia, (2011).
[9] I.D. Olekseyuk, I.V. Dudchak, L.V. Piskach, Phase equilibria in the Cu2S-ZnS-SnS2 system, Journal of Alloys and Compounds, 368 (2004) 135-143.
[10] T. Shimada, K. Oishi, K. Jimbo, H. Katagiri, H. Araki, O. Yoshida, M. Yamazaki, S. Kobayashi, N. Tsuboi, Crystal growth of Cu_2ZnSnS_4 by melting method, in: IEICE Technical report, 2005.
[11] M. Lachab, A.A. Attia, C. Llinarès, Study on the properties of CuInSe2 ingots grown from the melt using stoichiometric and non-stoichiometric charges, Journal of Crystal Growth, 280 (2005) 474-482.
[12] H. Matsushita, T. Ichikawa, A. Katsui, Structural, thermodynamical and optical properties of Cu_2-II-IV-VI_4 quaternary compounds, Journal of Materials Science, 40 (2005) 2003-2005.
[13] G.P. Bernardini, P. Bonazzi, M. Corazza, F. Corsini, G. Mazzetti, L. Poggi, G. Tanelli, New data on the Cu_2FeSnS_4-Cu_2ZnSnS_4 pseudobinary system at 750°C and 550°C, European Journal of Minerals, 2 (1990) 219-225.
[14] G.H. Moh, L.A. Taylor, Laboratory techniques in experimental sulfide petrology, Neues Jahrbuch für Mineralogie - Monatshefte, (1971) 450-459.
[15] M. Altosaar, J. Raudoja, K. Timmo, M. Danilson, M. Grossberg, J. Krustok, E. Mellikov, Cu_2Zn_{1-x} Cd_x $Sn(Se_{1-y}$ $S_y)_4$ solid solutions as absorber materials for solar cells, Physica Status Solidi (a), 205 (2008) 167-170.
[16] K. Timmo, M. Altosaar, J. Raudoja, K. Muska, M. Pilvet, M. Kauk, T. Varema, M. Danilson, O. Volobujeva, E. Mellikov, Sulfur-containing Cu2ZnSnSe4 monograin powders for solar cells, Solar Energy Materials and Solar Cells, 94 (2010) 1889-1892.
[17] M. Altosaar, A. Jagomägi, M. Kauk, M. Krunks, J. Krustok, E. Mellikov, J. Raudoja, T. Varema, Monograin layer solar cells, Thin Solid Films, 431-432 (2003) 466-469.
[18] A. Nagaoka, K. Yoshino, H. Taniguchi, T. Taniyama, H. Miyake, Preparation of Cu2ZnSnS4 single crystals from Sn solutions, Journal of Crystal Growth, (2012).
[19] R. Nitsche, D.F. Sargent, P. Wild, Crystal growth of quaternary 1_2246_4 chalcogenides by iodine vapour transport, Journal of Crystal Growth, 1 (1966).
[20] W. Schäfer, R. Nitsche, Tetrahedral quaternary chalcogenides of the type Cu_2-II-IV-$S_4(Se_4)$, Materials Research Bulletin, 9 (1974).
[21] S. Levcenko, V.E. Tezlevan, E. Arushanov, S. Schorr, T. Unold, Free-to-bound recombination in near stoichiometric Cu_2ZnSnS_4 single crystals, Physical Review B, 86 (2012) 045206.
[22] K. Klosse, A new productivity function and stability criterion in chemical vapor transport processes, Journal of Solid State Chemistry, 15 (1975) 105-116.
[23] K. Klosse, P. Ullersma, Convection in a chemical vapor transport process, Journal of Crystal Growth, 18 (1973) 167-174.
[24] K. Böttcher, H. Hartmann, Zinc selenide single crystal growth by chemical transport reactions, Journal of Crystal Growth, 146 (1995) 53-58.
[25] K. Böttcher, H. Hartmann, R. Röstel, Influence of convection on zinc selenide single crystal growth by chemical vapour transport, Journal of Crystal Growth, 159 (1996) 161-166.
[26] K. Böttcher, H. Hartmann, D. Siche, Computational study on the CVT of the ZnSe–I2 material system, Journal of Crystal Growth, 224 (2001) 195-203.
[27] D. Siche, K. Böttcher, U. Rinas, H. Hartmann, Crystal growth of zinc selenide under µg-conditions, Journal of Crystal Growth, 244 (2002) 249-256.
[28] M.M. Faktor, I. Garrett, Growth of crystals from the vapour, Chapman and Hall, Ltd., London, 1976.
[29] R. Gruehn, R. Glaum, New Results of Chemical Transport as a Method for the Preparation and Thermochemical Investigation of Solids, Angewandte Chemie International Edition, 39 (2000) 692-716.
[30] M. Lenz, R. Gruehn, Developments in Measuring and Calculating Chemical Vapor Transport Phenomena Demonstrated on Cr, Mo, W, and Their Compounds, Chemical Reviews, 97 (1997) 2967-2994.

[31] B.I. Noläng, M.W. Richardson, The transport flux function - A new method for predicting the rate of chemical transport in closed systems: I. Theory, Journal of Crystal Growth, 34 (1976) 198-204.
[32] H. Schäfer, Chemical Transport Reactions, Academic Press Inc., 1964.
[33] I. Jandl, K.W. Richter, H. Ipser, Incongruent, time-dependent chemical vapour transport in multi-component systems: A case study in Cr-Ge-Si, Solid State Sciences, 13 (2011) 1108-1114.
[34] P. Prabukanthan, R. Dhanasekaran, Stoichiometric single crystal growth of $AgGaS_2$ by iodine transport method and characterization, Crystal Research and Technology, 43 (2008) 1292-1296.
[35] S. Schorr, H.-J. Hoebler, M. Tovar, A neutron diffraction study of the Stannite-Kesterite solid solution series, European Journal of Minerals, 19 (2007).
[36] K. Hönes, E. Zscherpel, J. Scragg, S. Siebentritt, Shallow defects in Cu_2ZnSnS_4, Physica B: Condensed Matter, 404 (2009) 4949-4952.
[37] S. Delsante, R. Raggio, G. Borzone, Phase relations of the Sm–Ni–Al ternary system at 500°C in the 40–100 at.% Al region, Intermetallics, 16 (2008) 1250-1257.
[38] L. Guen, W.S. Glaunsinger, A. Wold, Physical properties of the quarternary chalcogenides Cu2IBIICIVX4 (BII = Zn, Mn, Fe, Co; CIV = Si, Ge, Sn; X = S, Se), Materials Research Bulletin, 14 (1979) 463-467.
[39] P. Bonazzi, L. Bindi, G.P. Bernardino, S. Menchetti, A model for the mechanism of incorporation of Cu Fe and Zn in the Stannite-Kesterite series Cu2FeSnS4-Cu2ZnSnS4, Canadian Mineralogist, 41 (2003).
[40] D. Drouin, A.R. Couture, D. Joly, X. Tastet, V. Aimez, R. Gauvin, CASINO V2.42 - A Fast and Easy-to-use Modeling Tool for Scanning Electron Microscopy and Microanalysis Users, Scanning, 29 (2007) 92-101.
[41] A. Weber, R. Mainz, H.W. Schock, On the Sn loss from thin films of the material system Cu--Zn--Sn--S in high vacuum, Journal of Applied Physics, 107 (2010) 013516-013516.
[42] A. Klimova, V. Ananichev, M. Arif, L. Blinov, Investigation of the Saturated Vapor Pressure of Zinc, Selenium, and Zinc Selenide, Glass Physics and Chemistry, 31 (2005) 760-762.
[43] S. Schorr, The crystal structure of kesterite type compounds: A neutron and X-ray diffraction study, Solar Energy Materials and Solar Cells, 95 (2011) 1482-1488.
[44] S. Schorr, G. Gonzalez-Aviles, In-situ investigation of the structural phase transitions in Kesterite, Phys. Status Solidi A, 206 (2009).
[45] R. Zuo, W. Wang, Theoretical study on chemical vapor transport of ZnS-I2 system. Part II: numerical modeling, Journal of Crystal Growth, 236 (2002) 695-710.
[46] F.W. Ostwald, Lehrbuch der Allgemeinen Chemie, Engelmann, Leipzig, 1896.
[47] A. Szczerbakow, K. Durose, Self-selecting vapour growth of bulk crystals : Principles and applicability, Progress in Crystal Growth and Characterization of Materials, 51 (2005) 28.
[48] H. Eyring, The Activated Complex in Chemical Reactions, The Journal of Chemical Physics, 3 (1935) 107-115.
[49] W.W. Piper, S.J. Polich, Vapor-Phase Growth of Single Crystals of II--VI Compounds, Journal of Applied Physics, 32 (1961) 1278-1279.
[50] E.V. Markov, A.A. Davydov, Izvestiya Akademii Nauk SSSR - Neorganicheskie Materialy, 7 (1971) 575.
[51] Handbook of Chemistry and Physics, 89th ed., CRC/Taylor and Francis, Boca Raton, 2009.
[52] L.I. Berger, B.R. Pamplin, Properties of semiconductors - Handbook of Chemistry and Physics, 89th ed., CRC/Taylor and Francis, Boca Raton, 2009.
[53] X. Fontané, L. Calvo-Barrio, V. Izquierdo-Roca, E. Saucedo, A. Perez-Rodriguez, J.R. Morante, D.M. Berg, P.J. Dale, S. Siebentritt, In-depth resolved Raman scattering analysis for the identification of secondary phases: Characterization of Cu_2ZnSnS_4 layers for solar cell applications, Applied Physics Letters, 98 (2011) 181905-181903.
[54] P.A. Fernandes, P.M.P. Salomé, A.F. da Cunha, Growth and Raman scattering characterization of Cu2ZnSnS4 thin films, Thin Solid Films, 517 (2009) 2519-2523.